nature communications

Article

https://doi.org/10.1038/s41467-025-66478-1

Sequential Organic Ligand Modifications to Dedicatedly Restructure Grain Boundary and Surface of Perovskites

Received: 13 June 2025

Accepted: 7 November 2025

Published online: 13 December 2025

Check for updates

Sajjad Ahmad[1,2], Wajid Ali[3], Jiayun Sun[1], Biao Zhou[1], Zhengyan Jiang[1], Jiazhi Meng[4], Hao Wang[5], Guodan Wei[4] & Wallace C. H. Choy[1,2]

The durability of perovskite solar cells (PSCs) is substantially limited by defects and imperfect structures at grain boundaries (GBs) and grain surfaces (GSs) of perovskites, where common single-step ligand passivation struggles due to ligand heterogeneous distributions and distinct chemical environments. Herein, we demonstrate a two-step sequential dedicated-ligand (TSS-DL) strategy that selectively targets GBs and GSs through spatially resolved interactions of the dedicated ligands. We identified two classes of dedicated ligands, including Ligand X, notably 2,2-difluoroacetamide bromide (DFABr) for GBs to restructure them into stable 2D perovskites and suppress defects, and Ligand Y, featuring 4-aminopiperidinium dibromide ($4APPBr_2$) for GSs to create a rigid 2D perovskite overlayer that shields 3D perovskites from external stresses. TSS-DL-treated PSCs retain >93% of their power conversion efficiency (PCE) after 3,000 hours of operation and >90% after 4,000 hours under high humidity (>85% RH). By sequentially restructuring GBs and GSs using dedicated ligands, the work provides an effective way to overcome the instability of 3D PSCs while maintaining high performance.

There has been significant interest from industry and academia in three-dimensional (3D) perovskite solar cells (PSCs), among the most promising photovoltaic technologies[1,2]. as the power conversion efficiency (PCE) has dramatically risen to over 27% today[3–5]. However, intrinsic instability and longevity of PSCs under real-world conditions (e.g., high humidity, continuous light soaking, and high temperature) remain significant challenges due to high defect densities at the grain boundaries (GBs) and grain surfaces (GSs) of polycrystalline perovskite film[6,7]. These defects may include undercoordinated halogen ions (X^{-}) or Pb^{2+} ions, lead clusters, Pb^{I-} anti-site defects, I^{I-} or MA^{+}, FA^{+}, and Cs^{+} vacancies[8].

Various approaches have been reported to suppress these defects[2,6,8,9]. One of the recent attractive approaches is to use organic ammonium ligands that mostly form a 2D perovskite layer on 3D perovskite to not only passivate but also shield 3D perovskite surfaces from degradation induced by moisture and oxygen[10], passivating defects, and suppressing ion migration[8,9,11,12]. However, the stability of 2D perovskite overlayers will vary or even degrade under thermal stress, highly dependent on the rigidity of the 2D perovskite which is seldom studied[13,14]. Besides, those 2D overlayers or surface passivation commonly formed by a single-step ligand process fail to uniformly cover both perovskite GBs and GSs comprehensively, causing incomplete treatment and degrading device efficiency and stability[6,15]. More importantly, in many studies, perovskites with different GBs and GSs are often treated by one kind of ligand, and improvements in device performance observed may be due to passivating defects of GSs rather than addressing the issues of GBs[16].

[1]Department of Electrical and Electronic Engineering, The University of Hong Kong, Pokfulam Road, Hong Kong, China. [2]Material Innovation Institute for Life Sciences and Energy (MILES), Shenzhen, China. [3]Key Laboratory of Optoelectronic Devices and Systems of Ministry of Education and Guangdong Province, College of Physics and Optoelectronic Engineering, Shenzhen University, Shenzhen 518060, China. [4]Institute of Materials Research, Tsinghua Shenzhen International Graduate School, Tsinghua University, Shenzhen 518000, PR China. [5]State Key Laboratory of Ultra-intense Laser Science and Technology, Shanghai Institute of Optics and Fine Mechanics (SIOM), Chinese Academy of Sciences (CAS), Shanghai 201800, China. e-mail: chchoy@eee.hku.hk

Notably, GBs and GSs have distinct chemical properties and structural environments. GBs are a homogeneous junction with a narrow spatial gap. They exhibit higher defect densities due to the misalignment of crystal lattices, which can lead to localized states that trap charge carriers. In contrast, GSs are a heterogeneous junction[17–19]. They primarily interact with their adjacent layer materials, leading to chemisorption or physisorption processes that alter their surface states. Therefore, heterogeneous distributions of the ligand and distinct chemical environments in GBs and GSs necessitate spatially tailored passivation strategies by dedicated ligands/ligands. Particularly, penetrability is important for GB additives because it affects how well they penetrate and interact with the defects within the GBs[16,20]. However, existing works predominantly employ mixed ligands in a single step, which do not show the spatial resolution to address the different defect chemistries of GBs and GSs[21,22]. Consequently, it is highly desirable to develop a strategy that effectively suppresses defects at both GBs and GSs with distinct chemical and structural characteristics to enhance stability and performance.

In this work, we introduce a two-step sequential dedicated-ligand (TSS-DL) strategy to independently address the distinct defect chemistries of GBs and GSs through their spatially resolved interactions of the dedicated ligands. Two classes of dedicated ligands in our TSS-DL strategy, including Ligand X and Ligand Y, are designed to target these specific defects by forming stable 2D perovskites and restructuring the GBs and GSs defective sites that enhance the perovskite material's overall performance. In the first step, Ligand X represented by 2,2-difluoroacetamide bromide (DFABr) with a small size and three distinct functional groups, can effectively penetrate GBs and suppress buried multiple defects, resulting in the formation of 2D perovskites via the three distinct functional groups, preventing water infiltration at the GBs. In the second step, class Y ligands, especially 4-aminopiperidinium dibromide ($4APPBr_2$), predominantly suppress GS defects and form a rigid 2D perovskite overlay on top of 3D perovskites as a protective barrier, significantly improving the film's resistance to external stressors such as heat, light, moisture, and oxygen, thereby enhancing its overall stability. Importantly, we find that the sequence of this process not only reconfigures the structure of GBs and GSs with fewer defects but also enhances overall optoelectronic properties, reduces non-radiative recombination, and improves energy level alignment while reversing the TSS-DL sequence limits the structure reconfiguration, leading to considerable PCE and stability drop. Differently, the TSS-DL-treated devices demonstrate outstanding stability, retaining >93% of their initial PCE after 3000 hr. continuous operation at maximum power point (MPP) and over 4000 hr. under high humidity (>85% RH). Even under aggressive damp-heat testing (85 °C and 85% RH), they maintain 93% efficiency after 2600 hr. Overall, by restructuring GBs and GSs using the TSS-DL strategy, this work illustrates spatially resolving interactions between dedicated ligands that stabilize GBs and GSs independently, and overcomes the limitations of single-step treatment, achieving high efficiency and stability in PSCs.

Results

Restructure perovskites by two-step sequential dedicated-ligand (TSS-DL) deposition

To address open-ended issues of various defects both at GBs and GSs (Fig. 1a), we propose the use of the TSS-DL strategy to ensure comprehensive coverage simultaneously both at the GBs and GSs of the perovskite film (detailed schematic procedure of this method is given in Supplementary Fig. 1)

While there are narrow dimensions of GBs and different chemistries than GSs, we explored various organic ligands that are not only highly penetrable but also multifunctionally address multiple defects in the GBs in the first step of TSS-DL (Fig. 1b). Interestingly, we find that certain ligands, designated here as Ligand X (notably DFABr), are particularly dedicated to GB defects and exhibit superior durability and performance when used as in the first step (Fig. 1c). In the second step we find that some ligands, referred to here as Ligand Y (notably 4APPBr) mainly passivate the GSs defects and achieve the best performance in the second step. Therefore, in the following discussion, we will delve deeper into the effects of these two ligands and the sequence of two steps of the TSS-DL strategy on 3D perovskite film and thus on optoelectronic properties, performance, and durability of PSCs.

We carefully applied each ligand in separate and sequential steps without prior mixing before deposition (Supplementary Fig. 2). This technique contrasts with traditional methods, where ligands are often mixed before deposition using single-step treatment, which can lead to uncontrolled interactions and aggregation. By applying each ligand separately and sequentially, we precisely control the distinct chemistries of GBs and GSs and achieve a more uniform and effective suppression of multiple defects simultaneously. While optimizing the TSS-DL strategy, the selection of appropriate ligands is critical to achieve the targeted stabilization of GBs and GSs. Both DFABr and 4APPBr were identified from the Ligand X and Ligand Y groups in Fig.1b based on their distinct chemical properties, which align with the specific stabilization needs of GBs and GSs, respectively. DFABr was selected as Ligand X for its ability to effectively target GBs due to its strong bonding capabilities via triple functional groups and small molecular size configuration (Supplementary Fig. 3), which allows it to penetrate and adhere to the narrow GBs more effectively[23–25]. This configuration facilitates the precise alignment of DFABr molecules, enhancing their interaction with GBs and acting as an all-in-one ligand[24]. As a result, DFABr can significantly reduce multiple defect sites at GBs, improve intrinsic stability and overall efficiency and stability. 4APPBr was chosen as Ligand Y, due to its rigid backbone that can selectively interact with GSs, forming a rigid 2D perovskite passivating layer that enhances structural stability and minimizes surface degradation[26]. By restructuring GSs, 4APPBr ensures that GSs remain stable over time, maintaining their performance. This complementary action with DFABr targeting of GBs ensures comprehensive defect management and long-term efficiency improvement of the PSCs. The detailed explanations of the effects of different ligands and their sequence in the treatment will be described below.

We first conducted time-of-flight secondary ion mass spectrometry (TOF-SIMS) to understand the penetration of ligands into the perovskite film. In the Perovskite/X/Y sample, X ligands are predominantly detected throughout the thickness of the perovskite films, while Y Ligands are principally detected on the surface (Fig. 2a). As a result, X ligands can uniquely penetrate the GBs. In the perovskite/Y/X, both ligands are distributed on the surface (Fig. 2b)[6]. This notable observation can be attributed to the steric hindrance, which is significantly larger in the Y cation due to its bulky ring structure. The bulky ring structure of the Y cation limits its ability to penetrate deeper into the film, causing it to remain primarily on the surface. On the other hand, the X cation, characterized by its smaller size and electron-withdrawing CF_2 group, is induced to penetrate profoundly within the GBs[27]. However, in the Perovskite/Y/X sample, the Y cation obstructs this deep penetration of the X cation.

Meanwhile, we employed X-ray photoelectron spectroscopy (XPS) to verify potential chemical interactions between Ligand X and Ligand Y with the perovskite structure, and to elucidate their sequential effects at GBs and GSs. When Ligand X, which contains O and F groups, introduced prior to Ligand Y, the Pb 4f peaks exhibited a more substantial shift toward lower binding energy (by 0.23 eV), suggesting increased electron density at Pb^{2+}, likely due to direct coordination with the oxygen and fluorine atoms in Ligand X (Fig. 2c). Additionally, the F 1s and O 1s peaks shifted to higher binding energies (Fig. 2d and Supplementary Fig. 4), indicating that these atoms are involved in strong chemical bonding with Pb^{2+} or other positively charged defects[28]. This pronounced shift in the XPS spectra when

https://doi.org/10.1038/s41467-025-66478-1

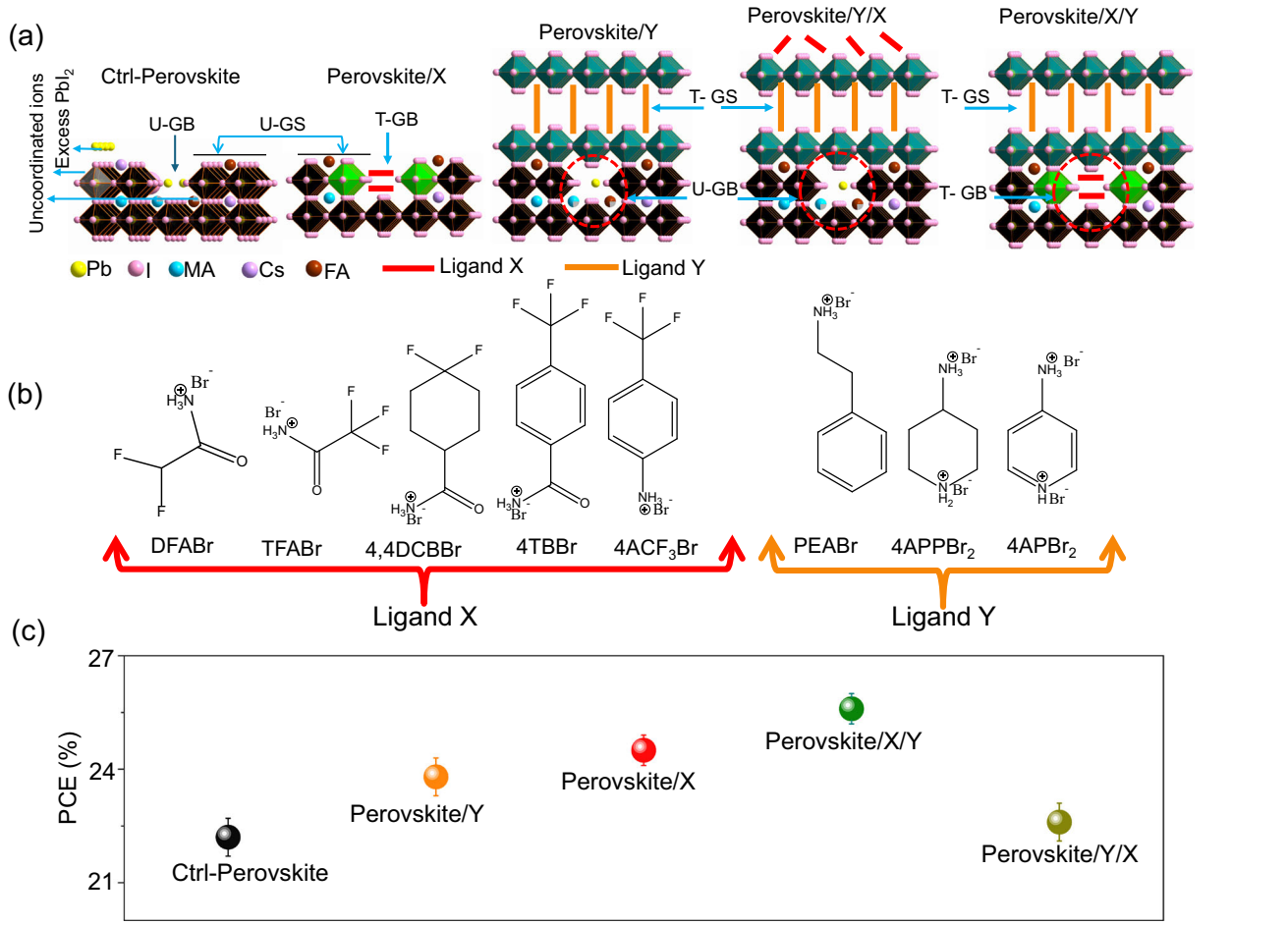

Fig. 1 | TSS-DL schematic illustration. a Schematic illustration showing perovskite GBs and GSs of control perovskites (Ctrl-Perovskite) treated with Ligand X only (Perovskite/X), Ligand Y only (Perovskite/Y), Ligand X and then Ligand Y (Perovskite/X/Y), and Ligand Y and then Ligand X (Perovskite/Y/X), where U-GB and U-GS mean untreated GB and GS, while T-GB and T-GS mean treated GB and GS. **b** Chemical structures of Ligand X and Ligand Y studied in this work, **c** PCEs of PSCs with untreated and treated perovskites.

Ligand X is applied first implies that Ligand X has a strong and direct chemical interaction with Pb^{2+} sites, which are abundant at GBs due to their higher defect density compared to GSs[16,23]. In contrast, (Perovskite/Y/X), less pronounced binding energy shifts for Pb 4f, O 1s, and F 1s were observed, suggesting that initial treatment of the perovskite film by Ligand Y at the GSs hinders subsequent interactions of Ligand X with the perovskite structure, particularly at the GBs.

To confirm the dedicated distributions of Ligand X at GBs and Ligand Y at GSs, local dark conductivity is assessed using conducting atomic force microscopy (c-AFM) to measure Ctrl-Perovskite and TSS-DL-treated perovskite films at designated locations, as the AFM topographic image in Fig. 2g. The GSs are denoted with square symbols, and the GBs are marked with triangular symbols. The tip bias is swept from 2.5 V to −2.5 V at a rate of 0.15 V/s. For the Ctrl-Perovskite, the observed dark currents at both GBs and GSs are the same as in previous reports[29,30] (Supplementary Fig. 5a). However, for the Perovskite/X, the dark current at the GSs is the same as the Ctrl-Perovskite, but at the GBs, the dark current is significantly higher by almost three times than that of the Ctrl-Perovskite (Figs. 2e and 2f). This indicates a substantial enhancement in conductivity at the GBs by Ligand X treatment, suggesting the successful incorporation of Ligand X at the GBs[31]. For the Perovskite/Y and Perovskite/X/Y samples, the dark currents at the GSs are markedly higher than those of the Ctrl-Perovskite and Perovskite/X samples (Supplementary Figs. 5b-7), confirming the predominant localization of Ligand Y at the GSs. Statistical analysis of dark current measurements taken at 40 different points in both the GBs and GSs for all samples is summarized in Fig. 2h, demonstrating the robustness and reproducibility of these results.

Kelvin Probe force microscopy (KPFM) is also used to analyze the effects of Ligand X and Y surface potential changes in perovskite films. The Ctrl-Perovskite film exhibited numerous GBs black pits (represented by white circles in Fig. 2g). A 1D height profile extracted from the topography indicates an average depth of ~70 nm between the GS and these pits (Supplementary Fig. 8). In the Perovskite/X, the number of black pits decreased significantly, and the average depth reduced to ~40 nm. While for the Perovskite/X/Y, nearly all pits were eliminated, with the average depth further reduced to ~20 nm. These results suggest that the TSS-DL method effectively fills the pits, indicating successful reconstruction of GBs and GSs sequentially. Moreover, the KPFM measurements showed a reduction in contact potential difference (CPD) from ~400 mV (Ctrl-perovskite) to ~150 mV for Perovskite/X and ~10 mV for perovskite//X/Y). This sharp decline in CPD correlates with the filling of GB pits, suggesting improved surface homogeneity. As a result, the Perovskite/X/Y sample displayed a uniform potential profile than both the Ctrl-perovskite and Perovskite/X. Consequently, the comprehensive suite of TOF-SIMS, XPS, c-AFM, and KPFM characterizations collectively demonstrates that the choice and sequence of ligand treatments profoundly influence the spatial distribution, chemical interaction, and electronic properties of the perovskite films. Specifically, ligand X, owing to its smaller size and electron-withdrawing properties, effectively penetrates and forms 2D perovskite to reconstruct GBs, enhancing local conductivity and

https://doi.org/10.1038/s41467-025-66478-1

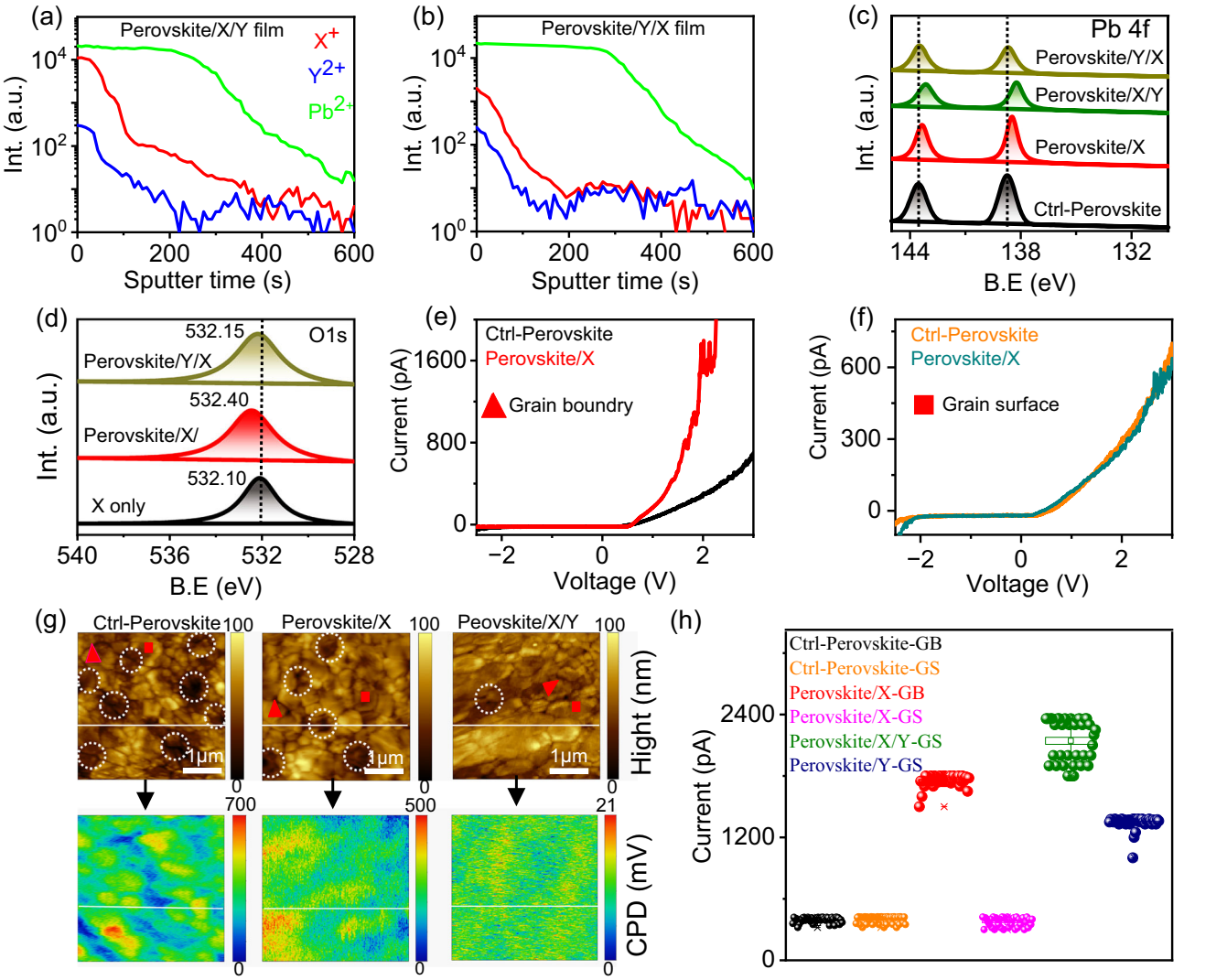

Fig. 2 | Ligands distribution. a, **b** TOP-SIMS spectra of Perovskite/X/Y and Perovskite/Y/X thin film. **c** Pb 4f XPS spectra of Ctrl-Perovskite, Perovskite/X and Perovskite/X/Y, Perovskite/Y/X and O 1s (**d**) XPS spectra of only X and Perovskite/X and Perovskite/Y/X film. Local dark currents measured at the GBs (**e**) and GS (**f**) of Ctrl-Perovskite and Perovskite/X thin film. **g** Topography and KPFM images of Ctrl-Perovskite, Perovskite/X and Perovskite/X/Y. **h** Statistical local dark-current distribution collected from 40 points at GBs and GSs of Ctrl-Perovskite, Perovskite/X, Perovskite/Y and Perovskite/X/Y (X= DFABr Y = 4APPBr).

passivating defect sites. Meanwhile, while the stability of 2D perovskite overlayers highly depends on its rigidity, the bulkier ligand Y is preferentially localized at the GSs, where it further forms rigid 2D perovskite to passivate surface defects as well as contributes to improved film uniformity[26]. Sequential application of X followed by Y enables complementary passivation of both GBs and GSs, resulting in reduced surface potential variations, enhanced electronic homogeneity, and overall superior film quality compared to either ligand alone or reversed treatment order.

Dedicatedly restructure grain boundaries and surfaces of perovskites

The effects of two classes of ligands, 'X' and 'Y', and their sequence on perovskite morphology and crystal structure are further investigated to understand how they restructure GBs and GSs and increase perovskite durability. The scanning electron microscopy (SEM) top-view and cross-sectional images reveal that Ctrl-perovskite films exhibit clear GBs (Fig. 3a). However, these GBs become almost imperceptible following a single-step deposition process using Ligand X (Supplementary Fig. 9), resulting in the formation of a dense, pinhole-free, and more uniform polycrystalline perovskite film, where the Ligand X predominantly modifies the GBs. We find that Perovskite/X film treated again with X ligand in the second step, there is no noticeable change, but its aggregate remains in the same position, as shown in Supplementary Fig. 10). Interestingly, when we treat the Perovskite/X sample again with Ligand Y (Perovskite/X/Y; Fig. 3a), it results in an even more uniform film with no visible GBs, suggesting that Ligand Y primarily passivates the GSs defects (Supplementary Fig. 11). To validate our findings, we examined the morphology of the Perovskite/Y/X film. In the Perovskite/Y/X sample, it is evident that the X ligand predominantly remains on top of the Perovskite/Y film without penetrating the GBs. It confirms that Ligand Y mainly modifies the perovskite GSs and highlights the importance of the sequence in imprinting the morphology uniformity.

To evaluate the crystallinity and modified structural properties of GBs and GSs after treatment, we conducted grazing-incidence wide-angle X-ray scattering (GIWAXS) measurements on TSS-DL-treated perovskite films and elucidated the sequential change of the two steps (Fig. 3a). The Ctrl-Perovskite film shows a distinct diffraction peak at q_z (~1.2 Å^{-1}), representing the (100) main peak of 3D perovskite with an intensive PbI_2 peak at q_z (~0.93 Å^{-1}). This excess PbI_2 on the 3D perovskite surface is beneficial for the 2D perovskite formation[9]. The diffraction map of the

https://doi.org/10.1038/s41467-025-66478-1

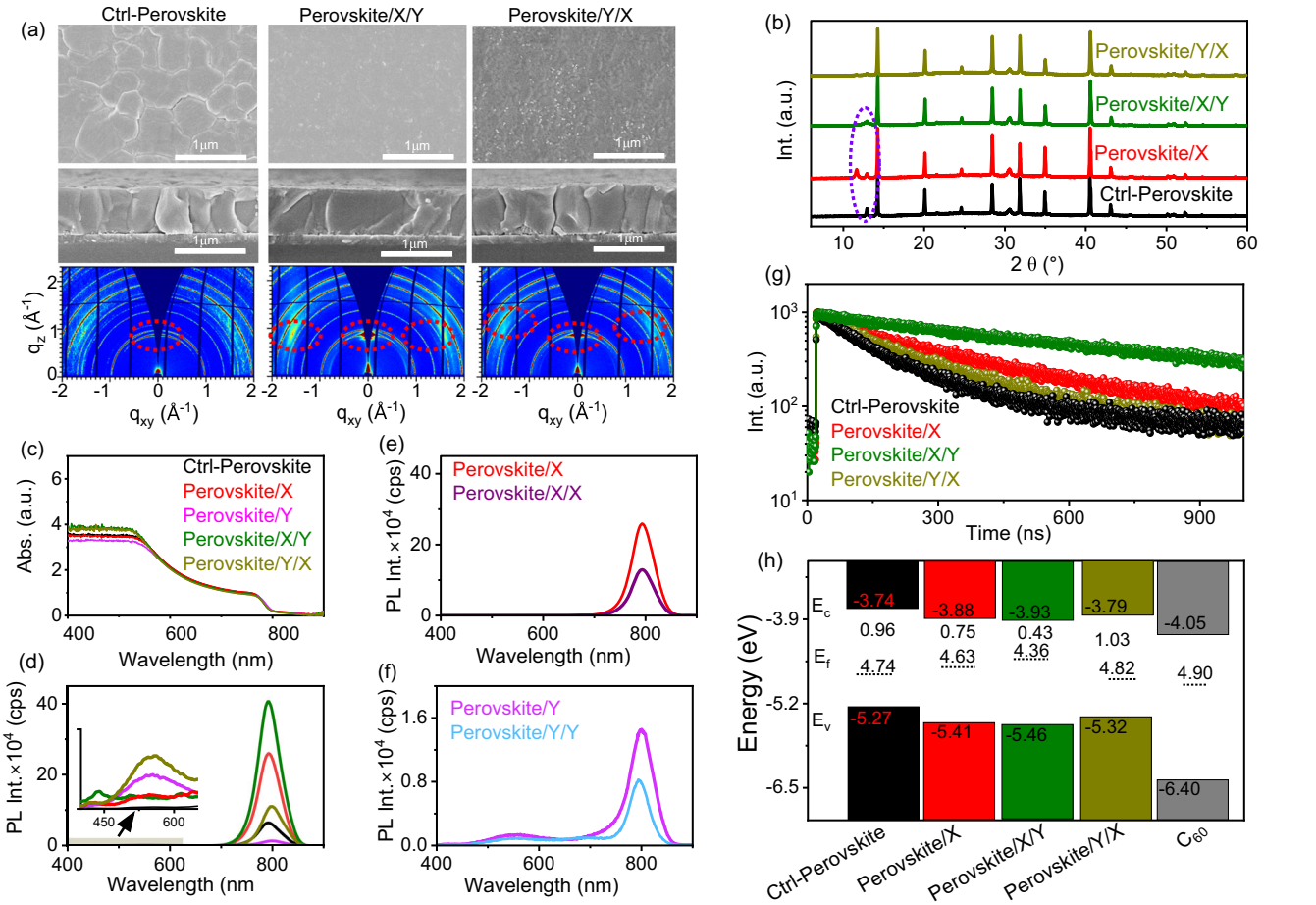

Fig. 3 | Crystallinity and optoelectronic properties. a Top view, cross-section SEM images and GIWAXS maps and XRD spectra (**b**) of Ctrl-Perovskite, Perovskite/X/Y and Perovskite/Y/X. **c** UV-Vis ((E_g= 1.55 eV)) and PL (**d**) spectra of Ctrl-Perovskite, Perovskite/X, Perovskite/Y, Perovskite/X/Y, and Perovskite/Y/X film. The inset shows the changes in the PL spectra at low wavelengths. Comparison of PL spectra for Perovskite/X and Perovskite/X/X (**e**) and Perovskite/Y and Perovskite/Y/Y (**f**). **g** TRPL spectra, and (**h**) Energy level diagrams of Ctrl-Perovskite, Perovskite/X, Perovskite/X/Y, and Perovskite/Y/X films.

Perovskite/X film (Supplementary Fig. 12) shows a weak PbI_2 peak and new strong diffraction peaks at lower q_z (~0.74 Å^{-1}) representing the (002) planes of the 2D perovskite at the GBs (n = 1)[9]. Stronger and additional discrete Bragg spots are observed at a higher q_z (q_z ~ 0.85 Å^{-1} and q_{xy} ~ 1.8 Å^{-1}) in the Perovskite/X/Y sample. This indicates the formation of an additional 2D perovskite phase with vertical orientation with respect to perovskite GSs corresponding to the (282), (121), and (082) planes, as highlighted with red dashed outlines. By contrast, we do not observe the difference between peaks at lower q_z and discrete Bragg spots in Perovskite/Y/X samples. However, the PbI_2 peak intensities in the Perovskite/Y/X sample are weaker than Perovskite/X/Y and show some passivation effect, but without additional Bragg spots covering some untreated defects at GBs. In addition, the GIWAXS results are consistent with conventional X-ray diffraction (XRD) analysis (Fig. 3b), where a small low-angle peak at 11.50° can also be observed for Perovskite/X (Supplementary Fig. 13), further confirming the formation of 2D perovskite structures. Furthermore, the high-resolution transmission electron microscopy (HR-TEM) of the Perovskite/X/Y sample also confirmed the formation of well-oriented 2D perovskite (Supplementary Fig. 14). This well-oriented structure is crucial for enhancing the material's optoelectronic properties, such as improved charge transport and reduced energy loss.

Optoelectronic properties of TSS-DL-treated perovskite

We investigate the potential for defect suppression and enhancement of charge carrier dynamics at the GBs and GSs in TSS-DL-treated perovskite films by examining their absorption and photoluminescence (PL) emission properties. UV-visible spectroscopy measurements (Fig. 3c) revealed that X ligands did not significantly alter the UV-vis absorption spectra after a single-step treatment, while Y ligand treatment in the first step resulted in decreased absorption. This highlights the importance of using X ligands in the first step. When Y ligands are applied in the second step, the Perovskite/X/Y absorption improves, indicating high-quality perovskite films. Furthermore, the PL intensity of Perovskite/X improved noticeably compared to the Ctrl-Perovskite and Perovskite/Y, suggesting a significant reduction in defects, and suppressed non-radiative charge recombination primarily at the GBs (Fig. 3d). Notably, for perovskite/X/Y the PL intensity further increased, and the low-wavelength peak shifted to 620 nm, indicating the possible presence of a mixture of two types of 2D perovskites (Fig. 3d inset)[32–36]. Conversely, for perovskite/Y/X the PL intensity also improved but much weaker than Perovskites/X/Y. Additionally treating with the same ligand in the second step also did not improve PL intensities (Fig. 3e and 3f), further confirming the importance of sequential deposition of ligand X and Ligand Y. Furthermore, the low-wavelength peak at 555 nm for Perovskite/X and at 620 nm for Perovskite/X/Y can also be observed from the back side, although with relatively weaker intensity compared to the front side (Supplementary Fig. 15). This observation confirms that Ligand-X predominantly penetrates at the GBs. In contrast, for the Perovskite/Y and Perovskite/Y/X samples, no low-wavelength peak is observed from the back side, suggesting that the Ligand-Y primarily reacts at the GSs and forms a 2D

https://doi.org/10.1038/s41467-025-66478-1

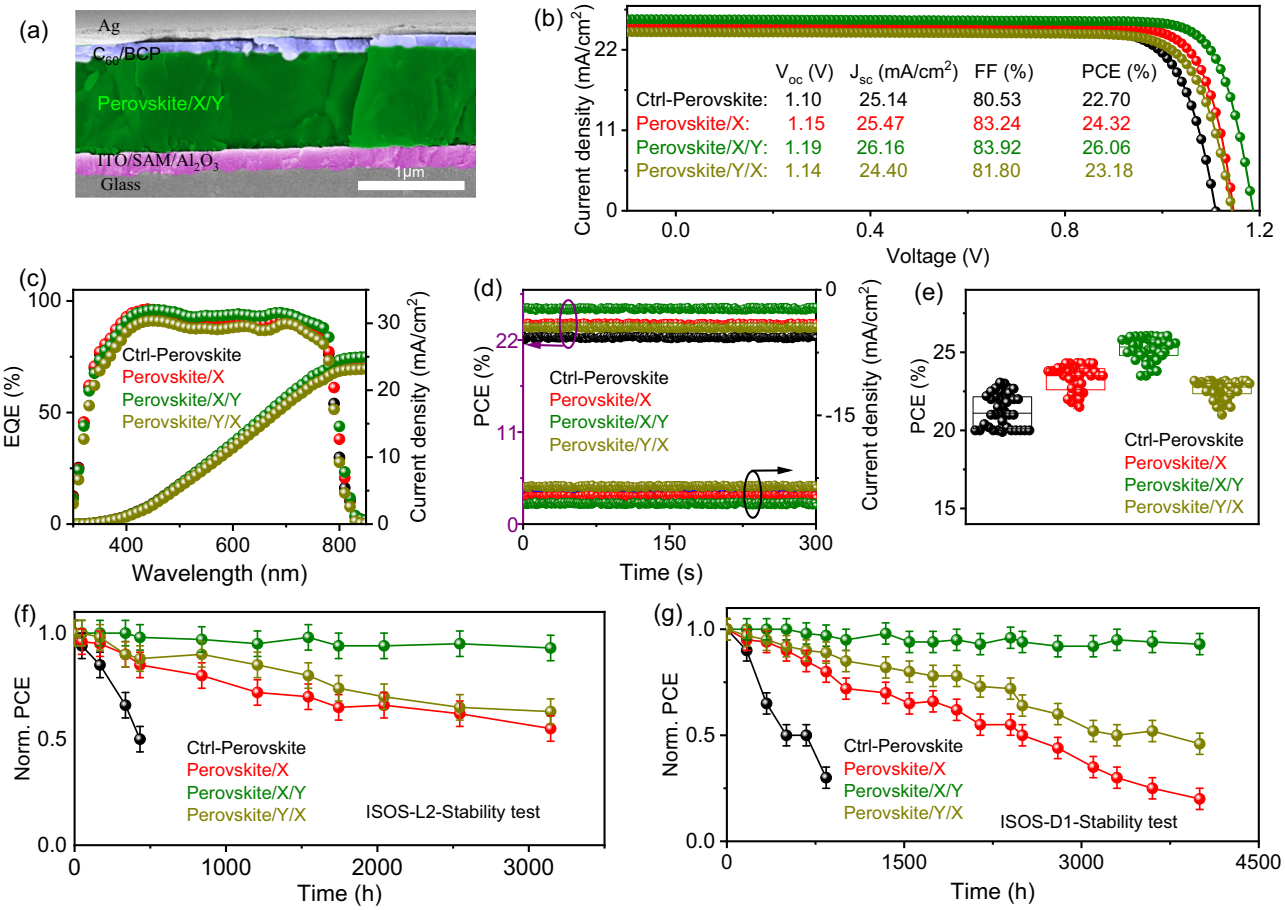

Fig. 4 | Device performance and stability. Cross-section SEM image of the champion device fabricated in this work (**a**), J-V curves (**b**) EQE spectra with integrated J_{sc} (**c**), stabilized performances (**d**) and histogram of 40 devices (**e**) of Ctrl-Perovskite, Perovskite/X, Perovskite/X/Y, and Perovskite/Y/X-based devices.ISOS-L2-operational stability at MPP at 65 °C for over 3000 hours (**f**) and ISOS-D1-long term dark storage stability in ambient environment (**g**) of Ctrl-perovskite, Perovskite/X, Perovskite/X/Y, and Perovskite/Y/X-based devices.

perovskite layer at the top. These results also align with the above c-AFM, SEM, XPS, and GIWAXS findings. To further validate the steady-state PL results, we conducted photoluminescence quantum yield (PLQY) measurements, which provide absolute values of emission efficiency. As shown in Supplementary Fig. 16, the PLQY of Perovskite/X/Y increased from 8.1% in the Ctrl- Perovskite and 13.1% in Perovskite/X to 17.8% in Perovskite/X/Y. In contrast, Perovskite/Y/X exhibited a reduced PLQY of 11.5%. These results indicate that non-radiative recombination was significantly suppressed by employing the TSS-DL method[37].

A time-resolved photoluminescence (TRPL) measurement is further conducted to examine the effects of the TSS-DL method on the charge carrier dynamics properties of perovskite films (Fig. 3g). The emission decreased sharply in the Ctrl-Perovskite films due to non-radiative carrier recombination at the GBs and GS. Upon single-step treatment (Perovskite/X), there is only a slight improvement in carrier lifetime, attributed to its ability to suppress defect-induced recombination at the GB. In contrast, the TSS films (Perovskite/X/Y) exhibited a significantly slower emission decay, indicating reduced nonradiative recombination at both GB and GS. These results suggest that the TSS-DL method effectively enhances the optoelectronic properties by improving carrier lifetime.

Finally, we explored the impact of the TSS-DL method on interface energy using ultraviolet photoelectron spectroscopy (UPS) (Fig.3h and Supplementary Fig. 17). The Perovskite/X/Y sequence also resulted in a significant reduction of the work function. This adjustment caused an upshift in the Fermi level and a downshift in the conduction band minimum (CBM), leading to an excellent alignment of energy levels with C_{60}. Consequently, this facilitated efficient electron-selective charge transfer[38]. Additionally, a deeper valence band maximum (VBM) can reduce electron-hole recombination at the interface by blocking hole transport. In contrast, Perovskite/Y/X sequences caused Fermi-level downshifts and CBM upshifts, resulting in a significant barrier to electron transport at the perovskites/C_{60} interface. These results further highlight the importance of introducing these ligands in the correct order.

Photovoltaic performances and stability

We further conducted an in-depth study on the effect of the TSS-DL strategy on device performance. Fig. 4a illustrates cross-sectional SEM images of p-i-in champion devices fabricated by this method. The J-V curves of champion devices are shown in Fig. 4b. As discussed above, initially, we evaluated all ligands first in the sept-I and then in step-II. We find that Ligand X, especially $DFABr_2$ at a concentration of 2 mg mL^{-1}, exhibits the best performance in the first step (Supplementary Fig. 18a and Supplementary Table 1). In the second step, Ligand Y, especially 4APPBr at 0.4 mg mL^{-1}, demonstrates superior efficacy (Supplementary Fig. 18b and Supplementary Table 2). Ctrl-Perovskite-based devices show a PCE of 22.52%, a V_{oc} of 1.10 V, a short-circuit current density (J_{sc}) of 25.14 mA/cm^2, and a fill factor (FF) of 80.53%. In contrast, the Perovskite/X-based devices exhibit an improved PCE of 24.23% with a V_{oc} of 1.15 V, a J_{SC} of 25.47 mA/cm^2, and an FF of 83.24%. Compared to Ctrl-Perovskite and Perovskite/X-based PSCs, Perovskite/X/Y-based devices have shown further improvements, achieving a

champion PCE of 26.06%. This was primarily due to enhancements in V_{oc} at 1.19 V, J_{sc} at 26.16 mA/cm², and FF at 83.92%. Interestingly, when changing the sequence, the PCE of the Perovskite/Y/X-based PSCs drops, with a maximum PCE of 23.18%, a J_{sc} of 24.4 mA/cm², and an FF of 81.8%. The external quantum efficiency (EQE) spectra shown in Fig. 4c provide integrated J_{sc} values that are comparable to those obtained from the J-V curves. Fig. 4d illustrates the stabilized performance of four types of photovoltaic devices, while Fig. 4e presents a statistical analysis of the PCEs of 40 devices of each type, confirming their reproducibility. The champion devices based on perovskite/X/Y also exhibited negligible hysteresis when measured in both the reverse and forward scan directions (Supplementary Fig. 19). To evaluate the feasibility of large-scale production of PSCs, 1 cm² devices are frequently employed as an intermediate step toward scaling up the device area[39–41]. Supplementary Fig. 20 shows the J-V curve of the champion device based on Perovskite/X/Y with an active area of 1 cm². A champion PCE exceeding 24% was achieved using our TSS-DL method, further demonstrating its scalability.

To evaluate the effect of the TSS-DL method on device stability, we further conducted three different types of standardized stability tests on our unencapsulated devices following the ISOS (International Summit on Organic PV Stability) protocols[42]. We investigate the stability of unencapsulated devices under continuous light illumination at MPP aging at 65 °C in ambient air with over 85% RH (ISOS-L2). The Perovskite/X/Y-based device retains over 93% of its initial PCEs after 3000 hr. of continuous operation, whereas the Ctrl-Perovskites, Perovskite/X, and Perovskite/Y/X devices show efficiency losses of over 20%, 30%, and 40% respectively (Fig. 4f). Additionally, we conducted a damp heat test at 85 °C and 85% RH (ISOS-D3), inside a humidity chamber (Supplementary Fig. 21). The Perovskite/X/Y-based device retained 94% of its maximum PCE after 2600 hours, compared to Perovskite/X, and Perovskite/Y/X devices, which retained only 20%, 40%, and 60% of their efficiencies, respectively. Moreover, the Perovskite/X/Y-based device demonstrated no efficiency degradation after even 4000 hr. of dark storage in ambient air at room temperature (ISOS-D1) (Fig. 4g). To further assess the moisture stability of the perovskite/X/Y films, contact angle measurements were conducted using water droplets (Supplementary Fig. 22). The results showed an increase in contact angle from 42.62° for the Ctrl-Perovskite, to 53.77° for Perovskite/X, and up to 67.13° for Perovskite/X/Y, indicating that the TSS-DL treatment effectively enhances the hydrophobicity of the surface[1]. We then evaluated long-term moisture stability by exposing Ctrl-Perovskite, Perovskite/X, and Perovskite/X/Y films to ambient air with a relative humidity of 80-90%. After three months, the Ctrl-Perovskite film had completely turned yellow, while Perovskite/X exhibited a slight brown coloration. In contrast, the Perovskite/X/Y films retained their original pure black phase under the same conditions (Supplementary Fig. 23). These findings further highlight the superior moisture resistance of Perovskite/X/Y films compared to the Ctrl-Perovskite and Perovskite/X films. This suggests that the TSS-DL treatment confers enhanced protection against moisture-induced degradation in perovskite films.

Discussion

The improved performance and stability of the simultaneous restructuring of GBs and GSs sequentially and independently through dedicated organic ligands. DFABr, which contains three distinct functional groups (NH^{3+}, = O, and F) and has a small molecular size, plays a crucial role in this stability and performance enhancement. The small size facilitates the permeability of DFABr along the deep-shallow of GBs, while three functional groups facilitate the formation of strong chemical interactions with the perovskite structure at GBs, which not only reduces vulnerable defect sites but also strengthens the perovskite lattice structure. This results in improved water resistance and operational longevity of the material at high temperatures. Additionally, the small size of DFABr allows it to navigate the intricate lattice structure of the perovskite material effectively, ensuring comprehensive coverage and interaction with the GBs. This minimizes defects and enhances transport charge, thereby improving the overall stability and efficiency of PSCs. In the second step, 4APPBr creates a protective layer of highly rigid 2D perovskites on the GSs, protecting the 3D perovskite from moisture and oxygen attack and improving thermal and light stability. This protection prolongs the lifespan and overall performance of perovskite-based devices. Although, as expected, the additional step causes a minor increase in costs of approximately 0.14%/m² for the large-scale production. However, the improved stability and efficiency given by the TSS-DL method yield a substantial increase in energy output (Energy yield) of around 47.7% compared to the single-step (Supplementary Tables 3 and 4). Furthermore, the TSS-DL method results in a lower Levelized cost of electricity (LCOE) of approximately 32.1% and a more favourable energy payback time over the device's lifetime. Given these findings, we believe that the enhanced operational lifetime and performance of the TSS-DL method will significantly offset the slight increase in costs associated with large-scale production, ultimately leading to a more efficient and cost-effective solution[43].

In summary, we developed an innovative TSS-DL strategy to enhance the stability and performance of PSCs by addressing defects at two critical locations, including GBs and GSs of 3D perovskite film. We screened a series of organic ligands and identified two classes of dedicated organic ligands: those that target GBs defects (Ligand X), particularly DFABr, in the first step, and those that mainly suppress the GSs (Ligand Y), particularly 4APPBr, in the second step. We find that the success of this sequence depends on the unique physicochemical properties of each ligand. The small molecular size and multifunctional groups of DFABr enable its deep penetration into GBs. Within these GBs, it forms chemical bonds with undercoordinated defects, intrinsically stabilizing the lattice and blocking water penetration along the restructuring GBs into 2D perovskites. Subsequent treatment with rigid $4APPBr_2$ ligands allows it to suppress the GS defects and form a highly rigid 2D perovskite overlayer on 3D perovskite, shielding it from various external stresses such as humidity, light, heat, and oxygen attack. Critically, reversing the TSS-DL sequence (applying $4APPBr_2$ first) results in its bulky structure blocking DFABr from accessing the GBs, leaving GB defects unaddressed and reducing the PCE from 26.06% to 23%. The optimized sequence ensures full restructuring of both GBs and GSs. More importantly, the sequential strategy also ensures exceptional stability of PSCs, maintaining over 93% of the initial PCE after 3000 hours of continuous operation at MPP and 4000 hours under high humidity conditions (>85% RH). Even under stringent damp-heat conditions (85°C and 85% RH), the devices retain more than 90% of their original efficiency after 2600 hours. By independently suppressing defects and reconstructing GBs and GSs with appropriately selected molecules in the correct order, we have effectively mitigated issues both within the GBs and GSs. This strategy overcomes the limitations of conventional single-step treatments, offering a promising pathway to more efficient and durable PSCs.

Methods

Materials

Lead (II) iodide (PbI_2, 99.9%), 2,2-Difluoroacetamide (DFA, >98.0% GC), 2,2,2-Trifluoroacetamide (TFA, >98.0% GC), 4-Aminobenzotrifluoride ($4ACF_3$, >98.0% GC&T), 4-(Trifluoromethyl)benzamide (4TB, >98.0% GC), 4,4-Difluorocyclohexanecarboxamide (95%, 4,4-DCB), 4-Aminopyridine (4AP, >99.0% GC&T), and 4-Aminopiperidine (4APP, >99.0% GC&T) were all obtained from TCI. Formamidine iodide (FAI) was obtained from GreatCellsolar materials in Australia. Dimethyl sulfoxide (DMSO, extra dry, 99%), N,N-Dimethylformamide (DMF, extra dry, 99%), isopropyl alcohol (IPA), Chlorobenzene (CB, extra dry, 99.8%), Hydrobromic acid (HBr, 48 wt.% solution in H_2O and aluminum

oxide (Al_2O_3) nanoparticles (with a particle size of <50 nm, 20 wt.% solution in isopropanol) were all sourced from Sigma-Aldrich. $PC_{60}BM$ was acquired from Solarmer Energy, while C_{60} was purchased from Organtec Ltd in China. Bathocuproine (BCP) was obtained from Acros Organics in the USA, and silver pellets were sourced from Kurt J. Lesker, also in the USA. Additionally, cesium iodide (CsI), [4-(3,6-dimethyl-9H-carbazol-9-yl)butyl]phosphonic acid (Me-4PACZ), and phenethyl ammonium bromide (PEABr. 99.9%) were purchased from Xian Polymer Light Technology Corp in China. All chemicals were used as received, without any additional purification steps.

Organic salt synthesis. All organic salts/spacers in this work are synthesized by dissolving equimolar amounts of organic spacer precursors in 2 mL of deionized water/ethanol, then add equimolar amounts of HBr aqueous solution dropwise. After stirring for 2 hours at 0°C, the precipitate is obtained by rotary evaporation, washed three times with ethanol and ether, and finally dried in an oven at 60°C for 12 hours to obtain.

Device fabrication

Patterned Glass/ITO substrates (15 Ω sq-1) were consecutively cleaned by sequential ultrasonication for 30 minutes with ethanol, acetone, and then stored in ethanol for further use. The cleaned substrates were dried with a high-pressure Nitrogen gas flow and then treated with UV-ozone for 30 minutes (ITO site facing up) before being transferred into an N_2-filled glove box device for fabrication. Me-4PACz (SAM) (0.33 mg/ml) in IPA was spin-coated on the glass/ITO substrate at 4,000 rpm for 30 seconds and then annealed at 100 °C for 10 minutes. Subsequently, Al_2O_3 (diluted by taking 60 µl from the stock in 2450 µl IPA) was spin-coated on ITO/SAM at 5000 rpm for 30 seconds and then annealed at 100°C for 5 minutes.

Fabrication of TSS-DL-based perovskite film. $Cs_{0.05}(FA_{0.79}MA_{0.21})_{0.95}PbI_3$ (E_g 1.55 eV)-based perovskite precursors were prepared in the mixed solvent of DMF and DMSO with a volume ratio of 4:1. The precursors were then filtered by a 0.2 μm PTFE syringe filter before use. The mixed perovskite precursor was spin-coated on the ITO/SAM/Al_2O_3 layer at 1000 rpm for 8 s and 27 seconds for 6000 rpm, and 200 µL of CB was dropped onto the spinning samples at the 10th second of the second step to form a brown film. Then the film was annealed at 110 °C for 25 min. The film was cooled down before the next step. Next in step 1, Ligand-X (2 mg/mL) in IPA: DMSO (200:1) was spin-coated dynamically on ITO/SAM/Al_2O_3/perovskite at 5000 rpm and then annealed at 100 °C for 5 minutes. The same procedure was repeated in step 2 with class Y salt (0.4 mg/mL). Next, C_{60} (40 nm), BCP (8 nm) and 120 nm Ag were thermally evaporated on treated/untreated perovskite films under a vacuum of 2×10^{-6} Torr in the high-vacuum deposition system, with a device area of 0.08 cm^2 or 1 cm^2.

Device measurements

All fresh and aged device performance measurements, excluding MPP stability tests, were conducted inside a N_2-filled glove box to ensure controlled conditions. All current vs voltage (J-V) measurements were performed in both forward and reverse scan directions over the voltage range of −0.1 V to 1.2 V with a step size of 0.01 V and a scan rate of 100 mV/s. These measurements were carried out under standard 1 sun illumination (AM1.5 G) using an Enlitech solar simulator (SS-F5-3A) linked with a Keithley 2400 source meter. The light intensity was calibrated using a standard silicon solar cell (SRC-2020, Enlitech). The EQE was measured in ambient air using a solar cell spectral response system (QE-R, Enlitech).

Thin film characterizations

Ultraviolet-visible (UV-vis) absorption spectra of Ctrl-Perovskite, Perovskite/X, Perovskite/Y, Perovskite/X/Y and Perovskites/Y/X-based films were measured in air at room temperature using a Shimadzu UV-Visible Spectrophotometer (UV-2600). All films were prepared on Glass/ITO substrates. X-ray Diffraction analysis (XRD) of all perovskite films was measured using a Rigaku Smart Lab diffractometer with Cu Kα radiation (λ = 1.5406 Å) at a voltage of 40 kV and 200 mA currents. The scanning range was 5.0°−60° with a scan rate of 5°/min and 0.02°/step. The perovskite samples for XRD were prepared on cleaned Glass/ITO substrates and measured under ambient conditions without any additional protocol. X-ray Photoelectron spectroscopy (XPS) measurements were performed in an ultra-high vacuum analysis chamber with a base pressure of approximately 1×10^{-10} Torr. A monochromatic Al Kα X-ray source (photon energy = 1486.6 eV) was used for excitation. The photoelectron spectra were acquired using a hemispherical electron energy analyser (PHOIBOS 150, SPECS). The samples were prepared on cleaned glass/ITO substrates inside an N_2-filled glovebox. Following fabrication of perovskite films, the samples were transferred to the XPS facility in vacuum-sealed plastic bags and measured on the same day to minimize exposure to air and potential contamination. Ultraviolet photoelectron spectroscopy (UPS) measurements were performed using an ultrahigh vacuum surface analysis system equipped with a ULVAC-PHI 5000 VersaProbe III spectrometer and a helium I (He I, 21.2 eV) photon source. The samples were biased at −5 V during measurement. The pass energy was set to 5.0 eV to ensure high-resolution spectra. Calibration of the UPS system was conducted using a clean gold (Au) substrate before measurements. Time-of-flight secondary ion mass spectrometry (TOF-SIMS) analyses were conducted on a NanoTOF-II instrument (ULVAC-PHI, Japan) employing a Bi_3^+ primary ion beam (30 kV) for high-resolution spectral acquisition and an Ar^+ sputter beam (3 keV, 100 nA) for depth profiling. Grazing-incidence wide-angle X-ray scattering (GIWAXS) measurements were conducted at the BL03HB beamlines of the Shanghai Synchrotron Radiation Facility (SSRF), utilizing an X-ray energy of 10 keV (wavelength 1.2398 Å) with a PLATUS detector, which was positioned vertically from the sample. The experiment was set with a grazing incidence angle of 0.4° and an exposure time of 10 seconds. The perovskite films for GIWAXS measurement were prepared on a Glass/ITO substrate. The contact angles of all samples were tested by the JC2000C1 contact angle meter of Powereach at room temperature on the same day. 1.0 µl of deionized water droplets was dropped carefully onto the perovskite films. Kelvin probe force microscopy (KPFM) and conductive-atomic force microscopy (c-AFM) data were collected concurrently using an atomic force microscope (NT-MDT NTEGRA) on the same day. A Pt-coated tip (Pt thickness: 30-35 nm; tip height: 14-16 μm) was employed for these measurements. To minimize noise and moisture interference, nitrogen gas continuously flowed into the chamber during measurement. The steady-state photoluminescence (PL), Time-resolved photoluminescence (TRPL) spectra, and PL quantum yield (PLQY were measured using a fluorescence spectrophotometer (PicoQaunt Fluo Time 300). A laser diode with a peak wavelength of 405 nm was used as the excitation source. The films were measured from the front side of the sample (perovskite side). High-resolution SEM (Hitachi S-4800) and TEM (Thermo Scientific Talos F200X STEM) were used to observe the morphology of the perovskite films.

Stability measurement

The ISOS-L2 and ISOS-D3 stability tests were conducted by storing the devices in a humidity chamber equipped with precise humidity and temperature control, a calibrated LED light source providing one-sun illumination, and an automated device stability tracking system. This system utilized custom MATLAB software integrated with a Keithley 2635 source meter for real-time performance monitoring. For the ISOS-L2 test, the temperature was maintained at 65°C, with the chamber door left open to ambient air at a relative humidity of 85 ± 5%. The maximum power point (MPP) was set based on the V_{max} values measured under 1-sun illumination for fresh devices: Ctrl-Perovskite

(0.96 V), Perovskite/X (0.98 V), Perovskite/X/Y (1.03 V), and Perovskite/Y/X (1.01 V). All current vs voltage (J-V) measurements were performed over the voltage range of −0.1 V to 1.2 V with a step size of 0.01 V and a scan rate of 100 mV/s. For the ISOS-D3 (damp heat test), devices were exposed to a constant temperature of 85°C and relative humidity of 85%, with performance measurements taken at regular intervals to assess degradation under accelerated aging conditions. For dark storage (ISOS-D1), unencapsulated devices were stored in the dark under ambient conditions with a relative humidity of 85 ± 5%. Device performance was periodically monitored throughout the storage period to evaluate shelf-life stability. The J-V scanning parameters were kept consistent across all stability measurements. For each aging condition, three pieces were tested, each featuring five fingers, and the reported data represent the average performance of these devices.

Reporting summary

Further information on research design is available in the Nature Portfolio Reporting Summary linked to this article.

Data availability

All data supporting this work are available in the main text and the supplementary information. Source data are provided with this paper.

References

1. Suo, J. et al. Multifunctional sulfonium-based treatment for perovskite solar cells with less than 1% efficiency loss over 4,500-h operational stability tests. *Nat. Energy* **9**, 172–183 (2024).
2. Xiong, S. et al. Reducing nonradiative recombination for highly efficient inverted perovskite solar cells via a synergistic bimolecular interface. *Nat. Commun.* **15**, 5607 (2024).
3. https://www.nrel.gov/pv/cell-efficiency.html.
4. Liu, X. et al. Perovskite solar modules with high efficiency exceeding 20%: From laboratory to industrial community. *Joule* 102056 https://doi.org/10.1016/j.joule.2025.102056 (2025).
5. Green, M. A. et al. Solar Cell Efficiency Tables (Version 66). *Prog. Photovolt. Res. Appl.* **33**, 795–810 (2025).
6. Lin, R. et al. All-perovskite tandem solar cells with improved grain surface passivation. *Nature* **603**, 73–78 (2022).
7. Lin, Y. H. et al. A piperidinium salt stabilizes efficient metal-halide perovskite solar cells. *Science* **369**, 96–102 (2020).
8. Wu, G. et al. Surface Passivation Using 2D Perovskites toward Efficient and Stable Perovskite Solar Cells. *Adv. Mater.* **34**, 2105653 (2022).
9. Azmi, R. et al. Double-side 2D/3D heterojunctions for inverted perovskite solar cells. *Nature* **628**, 93–98 (2024).
10. Zhu, H. et al. Tailored Amphiphilic Molecular Mitigators for Stable Perovskite Solar Cells with 23.5% Efficiency. *Adv. Mater.* **32**, 1907757 (2020).
11. Ahmad, S. et al. Dion-Jacobson Phase 2D Layered Perovskites for Solar Cells with Ultrahigh Stability. *Joule* **3**, 794–806 (2019).
12. Najarian, A. M. et al. 2D Hybrid Perovskites Employing an Organic Cation Paired with a Neutral Molecule. *J. Am. Chem. Soc.* **145**, 27242–27247 (2023).
13. Perini, C. A. R. et al. Interface Reconstruction from Ruddlesden–Popper Structures Impacts Stability in Lead Halide Perovskite Solar Cells. *Adv. Mater.* **34**, 2204726 (2022).
14. Chakkamalayath, J., Hiott, N. & Kamat, P. V. How Stable Is the 2D/3D Interface of Metal Halide Perovskite under Light and Heat?. *ACS Energy Lett.* **8**, 169–171 (2023).
15. Park, S. M., Abtahi, A., Boehm, A. M. & Graham, K. R. Surface Ligands for Methylammonium Lead Iodide Films: Surface Coverage, Energetics, and Photovoltaic Performance. *ACS Energy Lett.* **5**, 799–806 (2020).
16. Jiao, H. et al. Perovskite grain wrapping by converting interfaces and grain boundaries into robust and water-insoluble low-dimensional perovskites. *Sci. Adv.* **8**, eabq4524 (2022).
17. Castro-Méndez, A. F., Hidalgo, J. & Correa-Baena, J. P. The Role of Grain Boundaries in Perovskite Solar Cells. *Adv. Energy Mater.* **9**, 1901489 (2019).
18. Chun, D. H. et al. Grain Boundary Healing of Organic-Inorganic Halide Perovskites for Moisture Stability. *Nano Lett.* **19**, 6498–6505 (2019).
19. Pols, M. et al. What Happens at Surfaces and Grain Boundaries of Halide Perovskites: Insights from Reactive Molecular Dynamics Simulations of $CsPbI_3$. *ACS Appl. Mater. Interfaces* **14**, 40841–40850 (2022).
20. Ni, Z. et al. Evolution of defects during the degradation of metal halide perovskite solar cells under reverse bias and illumination. *Nat. Energy* **7**, 65–73 (2022).
21. La-Placa, M. G. et al. Vacuum-Deposited 2D/3D Perovskite Heterojunctions. *ACS Energy Lett.* **4**, 2893–2901 (2019).
22. Chen, H. et al. Quantum-size-tuned heterostructures enable efficient and stable inverted perovskite solar cells. *Nat. Photonics* **16**, 352–358 (2022).
23. Zhang, J. et al. The Role of Grain Boundaries in Organic–Inorganic Hybrid Perovskite Solar Cells and its Current Enhancement Strategies: A Review. *Energy Environ. Mater.* **7**, e12696 (2024).
24. Yang, M., Tian, T., Feng, W., Wang, L. & Wu, W. Q. Custom Molecular Design of Ligands for Perovskite Photovoltaics. *Acc. Mater. Res.* **2**, 1141–1155 (2021).
25. Feng, W., Zhang, C., Zhong, J. X., Ding, L. & Wu, W. Q. Correlating alkyl chain length with defect passivation efficacy in perovskite solar cells. *Chem. Commun.* **56**, 5006–5009 (2020).
26. Ahmad, S. et al. High-Quality Pure-Phase MA-Free Formamdinium Dion-Jacobson 2D Perovskites for Stable Unencapsulated Photovoltaics. *Adv. Energy Mater.* **14**, 2302774 (2024).
27. Chen, R. et al. Reduction of bulk and surface defects in inverted methylammonium- and bromide-free formamidinium perovskite solar cells. *Nat. Energy* **8**, 839–849 (2023).
28. Chen, H. et al. Improved charge extraction in inverted perovskite solar cells with dual-site-binding ligands. *Science* **384**, 189–193 (2024).
29. Wu, W. Q. et al. Molecular doping enabled scalable blading of efficient hole-transport-layer-free perovskite solar cells. *Nat. Commun.* **9**, 1625 (2018).
30. Shao, Y. et al. Grain boundary dominated ion migration in polycrystalline organic-inorganic halide perovskite films. *Energy Environ. Sci.* **9**, 1752–1759 (2016).
31. Ma, C. et al. Facet-Dependent Passivation for Efficient Perovskite Solar Cells. *J. Am. Chem. Soc.* **145**, 24349–24357 (2023).
32. Li, W. et al. Efficient and stable mesoscopic perovskite solar cell in high humidity by localized Dion-Jacobson 2D-3D heterostructures. *Nano Energy* **91**, 106666 (2022).
33. Yang, X. et al. Efficient green light-emitting diodes based on quasi-two-dimensional composition and phase engineered perovskite with surface passivation. *Nat. Commun.* **9**, 2–9 (2018).
34. Jiang, J. et al. Rational design of Al2O3/2D perovskite heterostructure dielectric for high performance MoS2 phototransistors. *Nat. Commun.* **11**, 4266 (2020).
35. Zhang, T. et al. Stable and Efficient 3D-2D Perovskite-Perovskite Planar Heterojunction Solar Cell without Organic Hole Transport Layer. *Joule* **2**, 2706–2721 (2018).
36. Zhu, T. et al. High-Performance Ternary Perovskite–Organic Solar Cells. *Adv. Mater.* **34**, 2109348 (2022).
37. Ali, W. et al. Suppressed Non-Radiative Recombination in Formamidinium Lead Triiodide under Electric Activation. *ACS Appl. Mater. Interfaces* **16**, 67642–67650 (2024).

38. Azmi, R. et al. Damp heat-stable perovskite solar cells with tailored-dimensionality 2D/3D heterojunctions. *Science* **376**, 73–77 (2022).
39. Li, B. et al. Highly Efficient and Scalable p-i-n Perovskite Solar Cells Enabled by Poly-metallocene Interfaces. *J. Am. Chem. Soc.* **146**, 13391–13398 (2024).
40. Liu, C. et al. Two-dimensional perovskitoids enhance stability in perovskite solar cells. *Nature* **633**, 359–364 (2024).
41. Sun, A. et al. High Open-Circuit Voltage (1.197 V) in Large-Area (1 cm^2) Inverted Perovskite Solar Cell via Interface Planarization and Highly Polar Self-Assembled Monolayer. *Adv. Energy Mater.* **14**, 1–12 (2024).
42. Khenkin, M. V. et al. Consensus statement for stability assessment and reporting for perovskite photovoltaics based on ISOS procedures. *Nat. Energy* **5**, 35–49 (2020).
43. Peplow, M. Are perovskites the future of solar power?. *Nature* **623**, 2023 (2023).

Acknowledgements

We thank the project of the University Grant Council of the University of Hong Kong (grant No. 2302101786 and 2402101935), Materials Innovation Institute for Life Sciences and Energy (MILES), HKU-SIRI, General Research Fund (grant Nos. 17200021, and 17200823, 17310624 and 17304925) from the Research Grants Council of Hong Kong Special Administrative Region, China, and Innovation and Technology Fund (GHP/245/22SZ) from Innovation and Technology Commission of Hong Kong Special Administrative Region, China.

Author contributions

Conceptualization, S.A. and W.C.H.C.; Methodology, S.A., W.A., and H.W.; Formal Analysis, S.A., J.S., W.A., and B.Z.; Validation, S.A., B.Z., and Z.J; Investigation, S.A., J.M., and G.W.; Writing Original Draft, S.A.; Writing-Review & Editing, S.A. and W.C.H.C.; Supervision, W.C.H.C.

Competing interests

The authors declare no competing interests.

Additional information

Supplementary information The online version contains supplementary material available at https://doi.org/10.1038/s41467-025-66478-1.

Correspondence and requests for materials should be addressed to Wallace C. H. Choy.

Peer review information *Nature Communications* thanks Jiangzhao Chen, Efrain Ochoa Martinez, and the other, anonymous, reviewer(s) for their contribution to the peer review of this work. A peer review file is available.